



# In situ fabrication of nickel aluminum-layered double hydroxide nanosheets/hollow carbon nanofibers composite as a novel electrode material for supercapacitors

Fang He <sup>a</sup>, Zhibiao Hu <sup>b</sup>, Kaiyu Liu <sup>a,\*</sup>, Shuirong Zhang <sup>a</sup>, Hongtao Liu <sup>a</sup>, Shangbin Sang <sup>a</sup>

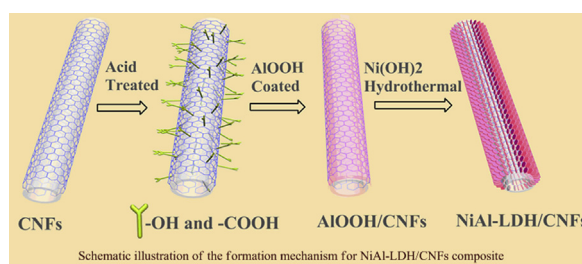
<sup>a</sup> College of Chemistry and Chemical Engineering, Central South University, Changsha 410083, China

<sup>b</sup> College of Chemistry and Material Science, Longyan University, Longyan 364012, China

## HIGHLIGHTS

- Nickel aluminum-LDH grown on hollow carbon nanofibers by an in situ growth method.
- NiAl-LDH/CNFs composite presents as three-dimensional network structure.
- The composite exhibited a high specific capacitance of 1613 F g<sup>-1</sup> at 1 A g<sup>-1</sup>.
- Remarkable cycle performance at a current density of 2 A g<sup>-1</sup>.

## GRAPHICAL ABSTRACT



## ARTICLE INFO

### Article history:

Received 22 March 2014

Received in revised form

3 May 2014

Accepted 17 May 2014

Available online 27 May 2014

### Keywords:

Nickel aluminum-layered double hydroxide

Hollow carbon nanofibers

Supercapacitors

Electrochemical performance

## ABSTRACT

This paper introduces a new design route to fabricate nickel aluminum-layered double hydroxide (NiAl-LDH) nanosheets/hollow carbon nanofibers (CNFs) composite through an in situ growth method. The NiAl-LDH thin layers which grow on hollow carbon nanofibers have an average thickness of 13.6 nm. The galvanostatic charge–discharge test of the NiAl-LDH/CNFs composite yields an impressive specific capacitance of 1613 F g<sup>-1</sup> at 1 A g<sup>-1</sup> in 6 M KOH solution, the composite shows a remarkable specific capacitance of 1110 F g<sup>-1</sup> even at a high current density of 10 A g<sup>-1</sup>. Furthermore, the composite remains a specific capacitance of 1406 F g<sup>-1</sup> after 1000 cycles at 2 A g<sup>-1</sup>, indicating the composite has excellent high-current capacitive behavior and good cycle stability in compared to pristine NiAl-LDH.

© 2014 Elsevier B.V. All rights reserved.

## 1. Introduction

The crisis of fossil fuels and deterioration of environment push our society to move towards sustainable and green energy. Supercapacitors (SCs), also known as electrochemical supercapacitors (ESCs) or ultracapacitors, have been attracting intensive attention for their high power density, environment non-toxicity, short

charge–discharge time, and long cycle life [1–3]. In general, SCs are divided into two types according to their energy storage mechanism: electrochemical double layer capacitors (EDLCs) and pseudocapacitors (PCs), which mainly arise from ions stored in the electrode/electrolyte interface and fast surface redox reactions, respectively. To fulfill the higher requirement of future systems, for example, to accomplish the task of high energy output for electric vehicle (EV) and hybrid electric vehicle (HEV), SCs can provide enough energy in a short time, this advantage makes SCs became one of the most promising systems for the next generation high-energy storage systems [4–6]. It is well known that carbon

\* Corresponding author. Tel./fax: +86 0731 88879616.

E-mail address: [kaiyuli67@263.net](mailto:kaiyuli67@263.net) (K. Liu).

materials (carbon nanotubes, graphene and activated carbon, etc.) are typical electrode materials for the EDLCs [7–9]. However, carbon materials have a small specific capacitance in spite of the better rate capability and long cycle life [10]. On the other hand, electrode materials with pseudo-capacitive properties have been intensively studied because of their large specific capacitance and fast redox kinetics, such as metal oxides ( $\text{RuO}_2$ ,  $\text{Co}_3\text{O}_4$ ,  $\text{NiO}$ ,  $\text{MnO}_2$ , etc.), conductive polymers (polyaniline, polypyrrole, polythiophene, etc.), and hydroxides ( $\text{Ni}(\text{OH})_2$ ,  $\text{Co}(\text{OH})_2$ , etc.) [11–19]. However, PCs have a low conductivity and poor cycle life due to the limited velocity of ion diffusion and electron transfer compared with EDLCs [20,21]. One effective approach to solve these problems is to combine PCs active materials with carbon materials to take full use of the advantages of pseudo-capacitance and double layer capacitance [2,22–25].

Materials with large surface area and highly ordered dimension are expected to exhibit superior performance potential in SCs [4,26,27]. Hollow carbon nanofibers (CNFs), which are relatively inexpensive compared with CNTs, with well arrangement of  $\text{sp}^2$  carbon layers, as its excellent electronic, thermal properties, and high electrical conductivity, are regarded as a promising electrode material for SCs [28–31]. Layered double hydroxides (LDH) have exhibited unique electrochemical properties when it used as PCs electrode materials [2,32]. They are usually present in a general formula of  $[\text{M}^{2+}_{1-x}\text{M}^{3+}_x(\text{OH})_2]^{+x}[(\text{A}^{n-})_{x/n}\cdot m\text{H}_2\text{O}]$ , where  $\text{M}^{2+}$  and  $\text{M}^{3+}$  are divalent and trivalent metal ions,  $x$  is defined as the molar ratio of  $\text{M}^{3+}/(\text{M}^{2+} + \text{M}^{3+})$  and generally has a value ranging from 0.2 to 0.33,  $\text{A}^{n-}$  are the interlayer anions [33–35]. LDH also have potential application in catalysts [36], precursors [37], environmental protection [38], and drug delivery [39], etc.

Recently, LDH and carbon materials composites have been investigated intensively as promising capacitive materials due to high redox activity, enhanced electrochemical performances, environmentally friendliness, and low cost [10,40,41], such as  $\text{NiAl-LDH/GNS}$  [42],  $\text{CoAl-LDH/MWCNT}$  [43],  $\text{CoAl-LDH/GO}$  [46]. For instance, Gao et al. prepared graphene nanosheet/ $\text{NiAl-LDH}$  composite through a hydrothermal process and the products provide a maximum specific capacitance of  $781.5 \text{ F g}^{-1}$  at  $10 \text{ mA cm}^{-2}$  in 6 M KOH solution [2]. Yang et al. reported MWCNT-doped  $\text{NiCoAl-LDH}$  nanohybrid by a simple urea precipitation method, the specific capacitance of the nanohybrid reaches  $1035 \text{ F g}^{-1}$  at  $1 \text{ A g}^{-1}$  in 6 M KOH solution [7]. However, the LDH and carbon materials composites used as active materials of SCs generally have low conductivity, inferior rate capability, and small specific capacitance. These features obstruct the application of SCs.

In this paper, we introduce a new protocol to fabricate the  $\text{NiAl-LDH/CNFs}$  composite using a situ growth method. As far as I know, this is the first example to obtain the  $\text{NiAl-LDH/CNFs}$  composite. In our experiments, the  $\text{NiAl-LDH}$  nanosheets were grown vertically on the surface of hollow carbon nanofibers to form the three-dimensional porous structure which is a key factor to combine the pseudo capacitive of  $\text{NiAl-LDH}$  with double layer capacitive of hollow carbon nanofibers, the linear CNFs can provide a stable network-like structure during the charge–discharge process, which can facilitate the fast electron transfer and decrease in electrochemical polarization of the active material. Therefore, the  $\text{NiAl-LDH/CNFs}$  composite can offer an excellent electrochemical performance.

## 2. Experimental section

### 2.1. Pretreatment of hollow carbon nanofibers

Hollow carbon nanofibers, with diameters of 100 nm, were purchased from Sigma–Aldrich, which is denoted as CNFs if there is

no special declaration in the following passage. The pristine CNFs were treated with a mixture of concentrated nitric acid and sulfuric acid (in a volume ratio of 1:3) by refluxing in a round-bottom flask for 6 h at  $80^\circ\text{C}$ . Then the modified CNFs were filtered and washed with deionized water until  $\text{pH} = 7$ . Finally, the collected powder was dried at  $60^\circ\text{C}$  for 12 h. As a result, a number of negatively charged carboxyl groups were introduced onto the surface of CNFs. The other reagents (analytical grade) were used as received without further purification.

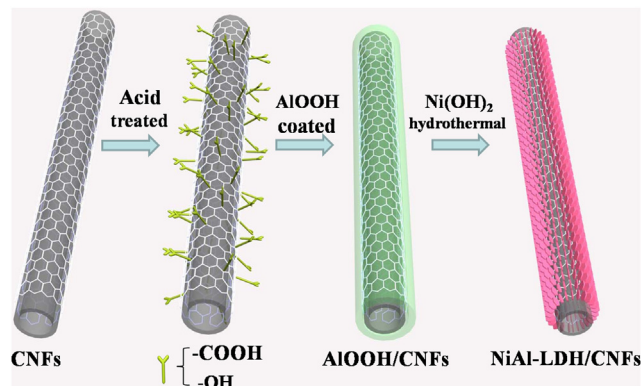
### 2.2. Synthesis of $\text{NiAl-LDH/CNFs}$ composite

The  $\text{NiAl-LDH/CNFs}$  composite was prepared via a situ growth method. Firstly, the boehmite primer ( $\text{AlOOH}$ ) sol was prepared by hydrolysis process. To be specific, 6 g aluminum isopropoxide ( $\text{Al}(\text{OPr})_3$ ) was added into  $\text{HNO}_3$  solution (50 ml, 0.05 M), followed by refluxing in a round-bottom flask for 6 h at  $90^\circ\text{C}$ . After that, the CNFs covered with  $\text{AlOOH}$  to form a shell structure. Typically, the prepared CNFs (0.1 g) were dispersed in 50 ml  $\text{AlOOH}$  primer sol for 24 h with vigorous agitation, followed by filtration, and then washed thoroughly with ethanol several times, after that dried at room temperature.

$\text{NiAl-LDH/CNFs}$  composite was carried out through an in situ growth method. The  $\text{AlOOH/CNFs}$  (0.1 g) powder was dispersed in 70 ml deionized water by vigorous stirring for 10 min. Then  $\text{Ni}(\text{NO}_3)_2 \cdot 6\text{H}_2\text{O}$  (0.003 mol) and urea (0.01 mol) were added into the above solution. After stirring for about 20 min, the mixed solution was transferred into an autoclave at  $100^\circ\text{C}$  for 48 h. Finally, the resulting  $\text{NiAl-LDH/CNFs}$  composite was separated by centrifugation, rinsed with ethanol and dried at room temperature. The whole synthesis process of the composite is depicted in Scheme 1. For comparison, the pristine  $\text{NiAl-LDH}$  was synthesized by an identical process to that of the composite without the introduction of CNFs.

### 2.3. Structural characterization

The structure of the obtained samples were characterized by X-ray diffraction (XRD, Rigaku) using  $\text{CuK}\alpha$  radiation at 40 kV and 250 mA,  $\lambda = 1.5406 \text{ \AA}$ . SEM investigations were performed using a Quanta FEG 250 field emission scanning electron microscope (FEI, Electron Optics, B.V). EDX analyses were performed using an EDAX system. TEM and HRTEM (JEM-2100F) were used to study the morphologies and microstructure properties of samples. Fourier transform-infrared measurements (FT-IR) (Thermo Electron Scientific Instruments, Nicolet 6700, America) were recorded on KBr



**Scheme 1.** Schematic illustration of the formation mechanism for  $\text{NiAl-LDH/CNFs}$  composite.

pellets with a PE Paragon 1000 spectrophotometer. The X-ray photoelectron spectra (XPS) were taken on a K-Alpha 1063 (Thermo Fisher) electron energy spectrometer using  $\text{MgK}\alpha$  X-ray source (1253.6 eV).  $\text{N}_2$  adsorption/desorption were measured at a liquid nitrogen temperature ( $-196^\circ\text{C}$ ) using a physisorption/chemisorptions analyzer (Quantachrome Nova Surface Area Analyzer). Prior to adsorption, the samples were dried and degassed by heating in a vacuum to  $200^\circ\text{C}$  for 5 h. The pore volumes were estimated from the desorption branch of the isotherms, applying the BJH method in the software package Quantachrome NovaWin.

#### 2.4. Preparation of electrodes and electrochemical measurements

The electrochemical properties of the samples were investigated at a three electrode system, in which the samples were used for the fabrication of working electrode, an  $\text{Hg}/\text{HgO}$  electrode was used as the reference electrode, a platinum foil was used as the counter electrode, and 6 M KOH solution was used as the electrolyte. The working electrodes were prepared by mixing active material (2 mg), acetylene black and polytetrafluoroethylene (PTFE) at a weight ratio of 80:15:5 with addition of a small amount of ethanol. After coating the above slurries on Ni foam ( $8\text{ mm} \times 8\text{ mm}$ ). Then the mixture was dried at  $60^\circ\text{C}$  overnight under vacuum. Before the test, the working electrodes were soaked in 6 M KOH for 12 h. The cyclic voltammograms (CV) were recorded on a CHI 660D electrochemistry workstation at room temperature ( $25 \pm 2^\circ\text{C}$ ) in 6 M KOH solution. The galvanostatic charge and discharge tests were recorded on Land battery test system (Wuhan, China). The electrochemical impedance spectroscopy (EIS) tests of all samples were examined on PARSTAT 2273-type electrochemical system (Princeton Applied Research) in 6 M KOH solution, and was performed with an ac amplitude of 5 mV in the frequency range of 10 mHz–100 kHz.

### 3. Results and discussion

#### 3.1. Microstructure characterizations

The XRD patterns of CNFs, NiAl-LDH, and NiAl-LDH/CNFs composite are shown in Fig. 1. The XRD pattern of CNFs has an obvious peaks at  $26.1^\circ$  (002), features a basal spacing of 0.34 nm. The XRD patterns of pristine NiAl-LDH exhibit the hydrotalcite-like characteristics, indexing to rhombohedral NiAl-LDH (JCPDS NO. 15-0087) in  $R_{3m}$  space group [44]. Compared with the NiAl-LDH, the intensity of the composite diffraction peaks becomes relatively weak,

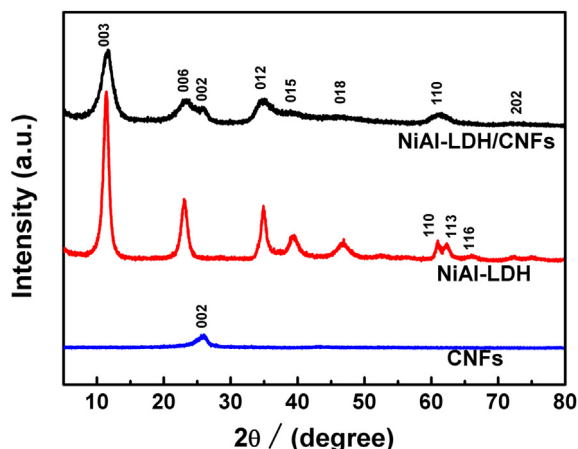


Fig. 1. XRD patterns of CNFs, NiAl-LDH, and NiAl-LDH/CNFs composite.

suggesting a low crystallinity of the composite. For the NiAl-LDH/CNFs composite, the basal spacing ( $d_{012}$ ) of NiAl-LDH in the nanocomposite is 0.26 nm. Moreover, the (002) diffraction peak of the CNFs is observed, a possible explanation is that we have obtained the NiAl-LDH/CNFs composite. This speculation is further confirmed by the SEM and TEM measurements.

The surface chemical composition of the CNFs, NiAl-LDH, and NiAl-LDH/CNFs composite were analyzed by FT-IR spectroscopy (Fig. 2). In the IR spectra of CNFs, NiAl-LDH, and NiAl-LDH/CNFs composite, the peaks at  $3445\text{ cm}^{-1}$  corresponding to the O–H stretching vibrations of water molecules and the hydrogen bonding of OH groups. The weak band at  $1625\text{ cm}^{-1}$  is due to the bending mode of water molecules [46]. For CNFs, the weak absorption bands around  $1709$  and  $1164\text{ cm}^{-1}$  corresponding to the vibration of C=O and C–O functional groups are observed, respectively. The peaks at  $1357$  and  $781\text{ cm}^{-1}$  are attributed to the  $\nu_3$  vibration and bending modes of the interlayer anion ( $\text{CO}_3^{2-}$ ), respectively, which was released from urea hydrolysis during the hydrothermal procedure [7,45]. The above analysis demonstrating the water molecules, and carbonate ions have been successfully intercalated into the interlayer space of NiAl-LDH during the assembly process. Other absorption bands below  $800\text{ cm}^{-1}$  are assigned to stretching and bending modes of the Metal–oxygen (M–O) in the hydrotalcite-like lattice [46].

To obtain further information about the chemical structures of NiAl-LDH and NiAl-LDH/CNFs composite, the as-prepared two samples were studied by XPS measurements. It can be clearly seen that the NiAl-LDH/CNFs composite is primarily composed of Ni, Al, C and O element in Fig. 3a. The appearance of Ni 2p XPS spectra of the composite is shown in Fig. 3b, there are two major peaks around 857.3 and 874.9 eV corresponding to Ni  $2p_{3/2}$  and Ni  $2p_{1/2}$  with a spin-energy separation of 17.6 eV that are characteristics of  $\text{Ni}^{2+}$  in  $\text{Ni}(\text{OH})_2$  [44,47]. In the C 1s XPS spectra of the NiAl-LDH/CNFs composite (Fig. 3c), the deconvolution of core-level C 1s spectrum of the composite refer to four types of carbon bonds: C=C ( $284.5\text{ eV}$ ), C–O ( $286.5\text{ eV}$ ), C=O ( $287.8\text{ eV}$ ) and O–C=O ( $289.0\text{ eV}$ ). It is interesting to find that the C=O peak appears in the NiAl-LDH/CNFs composite, suggesting the existence of oxygen-containing functional groups on the surface of CNFs in composite [2,7,44]. In addition, tiny amount of carbon was detected in the pure NiAl-LDH (Fig. 3d), argon sputtering was carried out on the NiAl-LDH with different times, the surface percentage of carbon decrease from 100% to 12.6% after sputtering of 990 s (Fig. 3e). In the core-level C 1s spectra of NiAl-LDH (Fig. 3f), two types of carbon bonds can be observed: C=C ( $284.5\text{ eV}$ ), O–C=O ( $289.0\text{ eV}$ ). With the increase of sputter time, the intensity of C=C peaks becomes

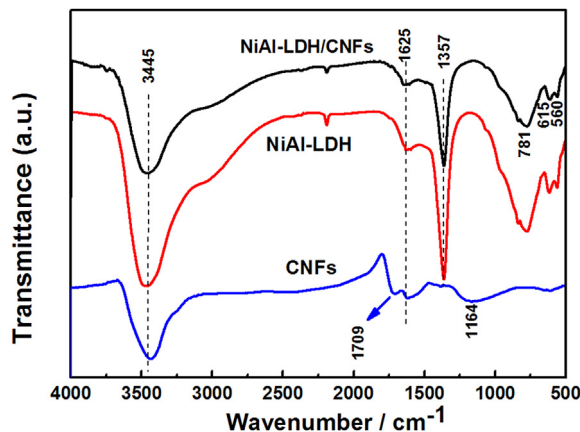
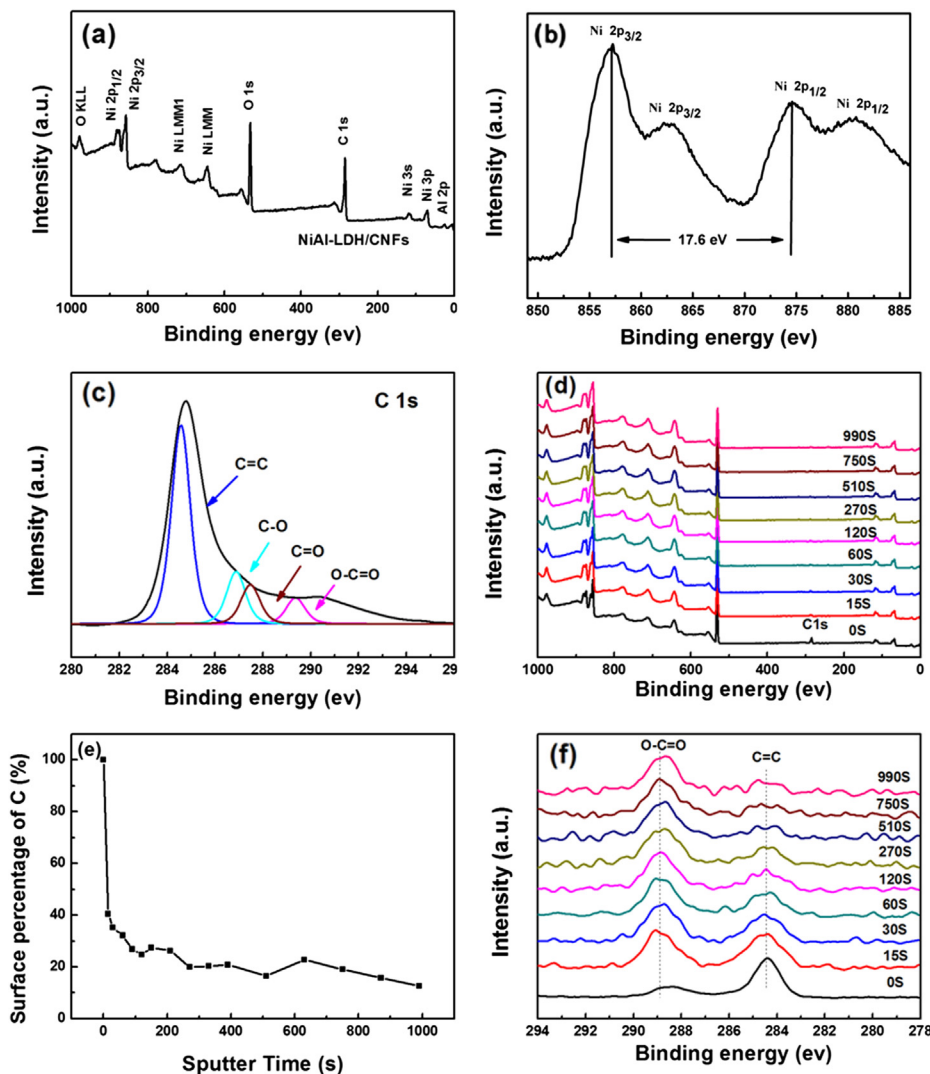


Fig. 2. FT-IR spectra of the CNFs, NiAl-LDH, and NiAl-LDH/CNFs nanocomposite.



**Fig. 3.** XPS spectra of NiAl-LDH/CNFs composite, the core-level Ni 2p of the composite (b), the core-level C1s spectra of NiAl-LDH/CNFs composite (c), XPS spectra of NiAl-LDH with different sputtering time (d), The surface percentage of C in NiAl-LDH with different sputtering time (e), The core-level C1s spectra of NiAl-LDH with different sputtering time (f).

relatively weak, suggesting the C=C of the sample was just adventitious carbon, for example, as the sample exposed in air or contact with other pollutants. On the other hand, the intensity of O–C=O ( $\text{CO}_3^{2-}$ ) peaks remains stable, indicating that  $\text{CO}_3^{2-}$  anion is the component of the NiAl-LDH, which is embedded into the interlayer of the stable LDH structure. These results are in agreement with the FT-IR results as mentioned above.

To examine the pore structures and the specific textural properties of NiAl-LDH, CNFs and NiAl-LDH/CNFs composite, the  $\text{N}_2$  adsorption/desorption isotherms and the corresponding pore size distributions are displayed in Fig. 4. All the curves exhibit typical IV isotherms with an H3-type hysteresis loop ( $P/P_0 > 0.4$ ), confirming the existence of mesopores in all samples [6,44]. The specific surface area of the composite ( $100.379 \text{ m}^2 \text{ g}^{-1}$ ) is higher than that of pristine NiAl-LDH ( $65.418 \text{ m}^2 \text{ g}^{-1}$ ) and CNFs ( $19.566 \text{ m}^2 \text{ g}^{-1}$ ), suggesting that the specific surface area of the composite is increased due to the addition of CNFs. The total pore volume of the composite increases to  $0.3569 \text{ cm}^3 \text{ g}^{-1}$ , while the total pore volume of NiAl-LDH and CNFs are  $0.1596 \text{ cm}^3 \text{ g}^{-1}$  and  $0.0298 \text{ cm}^3 \text{ g}^{-1}$ , respectively. The larger pore volume of the composite can be arises from the presence of CNF, which can decrease the aggregation of NiAl-LDH nanosheets. From the pore size distribution curves of all the

samples, NiAl-LDH displays pore size distribution of 14.2 nm, CNFs presents pore size distribution of 5.5 nm, while the NiAl-LDH/CNFs composite shows narrow size distribution (4.6 nm) after the introduction of CNFs. It has been reported that the pore size distribution within 2–5 nm is optimal for the behavior of capacitors [4]. Such a unique mesoporous structure can provide more efficient transport pathways to their interior voids, which is critical for their supercapacitor properties.

The SEM images of the pristine CNFs, NiAl-LDH, and NiAl-LDH/CNFs samples are shown in Fig. 5. These CNFs have diameters ranging from 100 to 200 nm according to Fig. 5a. From Fig. 5b, the image indicates that the NiAl-LDH consists of large amount of hexagonal flakes. From Fig. 5c–d, we can see that NiAl-LDH covered on CNFs. This observation is consistent with the following TEM images. In addition, the NiAl-LDH/CNFs composite was further examined by EDS, and the corresponding EDS spectra of the NiAl-LDH/CNFs composite in Fig. 5e. It demonstrates that the composite has Ni, Al, C, and O, which is corresponding to the NiAl-LDH and CNFs in the composite.

The microstructure of the synthesized NiAl-LDH/CNFs nanocomposite was observed with TEM image (Fig. 6a). The image indicates that the NiAl-LDH have grown vertically on CNFs through

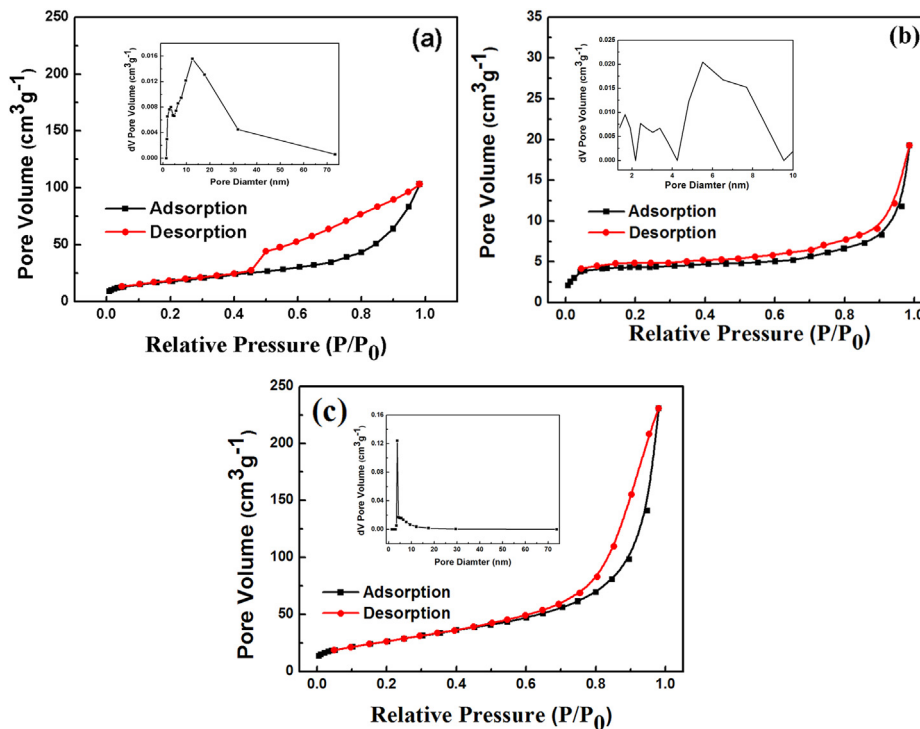


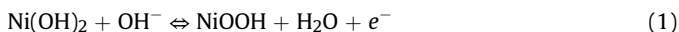
Fig. 4. The gas ( $N_2$ ) adsorption–desorption isotherm loop and the pore size distribution data for the synthesized NiAl-LDH (a), pristine CNFs (b) and NiAl-LDH/CNFs composite (c).

an in situ growth method. In addition, the TEM measurements indicate that those hexagonal platelet-like NiAl-LDH flakes in the composite are around 13.6 nm in thickness. From the high-resolution TEM (HRTEM) visualizations of the NiAl-LDH/CNFs composite (Fig. 6b), the clear lattice between the adjacent fringes are observed. The inter-planar distance of NiAl-LDH is measured to be 0.253 nm, corresponding to the  $d_{012}$  value of rhombohedral NiAl-LDH. Moreover, the inter-planar distance of CNFs is measured to be 0.34 nm, agreeing with the  $d_{002}$  value of carbon nanofibers, it is consistent with the above XRD results.

### 3.2. Electrochemical properties

The electrochemical behaviors of the as-prepared electrode materials were investigated by CV, galvanostatic charge–discharge measurements, and EIS.

Fig. 7a and b shows the typical CV curves of the NiAl-LDH/CNFs composite and pure NiAl-LDH electrodes within the potential window of 0.1–0.55 V (vs. Hg/HgO) in 6 M KOH solution at various scan rates from 5 to 50  $\text{mV s}^{-1}$ . There is always a pair of redox peak with an anodic peak at 0.43 V and a cathodic peak at 0.32 V, corresponding to the redox of  $\text{Ni}^{2+}/\text{Ni}^{3+}$  associated with  $\text{OH}^-$  [20,48]. This process can be described as shown in Equation (1).



The potential difference ( $\Delta E_{a,c}$ ) between the anodic and cathodic peaks is used as a measure of the reversibility of the electrochemical redox reaction: the smaller the  $\Delta E_{a,c}$ , the higher the reversibility. However, at different scanning rates, the potential difference ( $\Delta E_{a,c}$ ) between the anodic and cathodic peaks is higher than the theoretical value 59 mV, which means that the electrode is not reversible [2]. It can be seen from Fig. 7a that more than one peak in cathodic sweep. In comparison, the nickel foam as working

electrode was investigated by CV measurements, and the result displays a pair of redox peak with an anodic peak at 0.49 V and a cathodic peak at 0.30 V, corresponding to the extra peak in cathodic sweep. So we think the extra peak may be caused by the background signal of nickel foam [8]. All of the CV curves have a pair of symmetrical redox peaks, with almost ideal shapes, indicating that the charge and discharge processes of NiAl-LDH/CNFs composite are continuous and quasi-reversible. With the scan rate rises, the redox peak current density increased significantly, indicating the faster redox rate on the electrode. In addition, as the increase of polarization of active material, the potential difference ( $\Delta E_{a,c}$ ) between the anodic and cathodic peaks become larger (the peak potential of reduction turns negative, and the peak potential of oxidation turns positive), which implies the lower reversibility of the electrode [2,19].

Fig. 7c shows that at 30  $\text{mV s}^{-1}$  scan rate in 6 M KOH electrolyte, the NiAl-LDH/CNFs composite has a higher redox current intensity and a larger integral area of the CV curve compare to those of pure NiAl-LDH. This result demonstrates that the NiAl-LDH/CNFs composite has a higher specific capacitance which can be attributed to the high electrical conductivity and increased specific surface area by the effect of the CNFs addition. The relatively large surface area is favorable to the ion transport between the active materials and electrolyte, and the good electrical conductivity can promote the electron transfer in the faradic redox reaction [49].

To further investigate the electrochemical performance of electrode materials, galvanostatic charge/discharge tests of NiAl-LDH and NiAl-LDH/CNFs composite electrodes were conducted in 6 M KOH in different current densities in a voltage range of 0.1–0.55 V. The specific capacitances can be calculated according to Equation (2):

$$C_s = \frac{It}{(\Delta V)m} \quad (2)$$

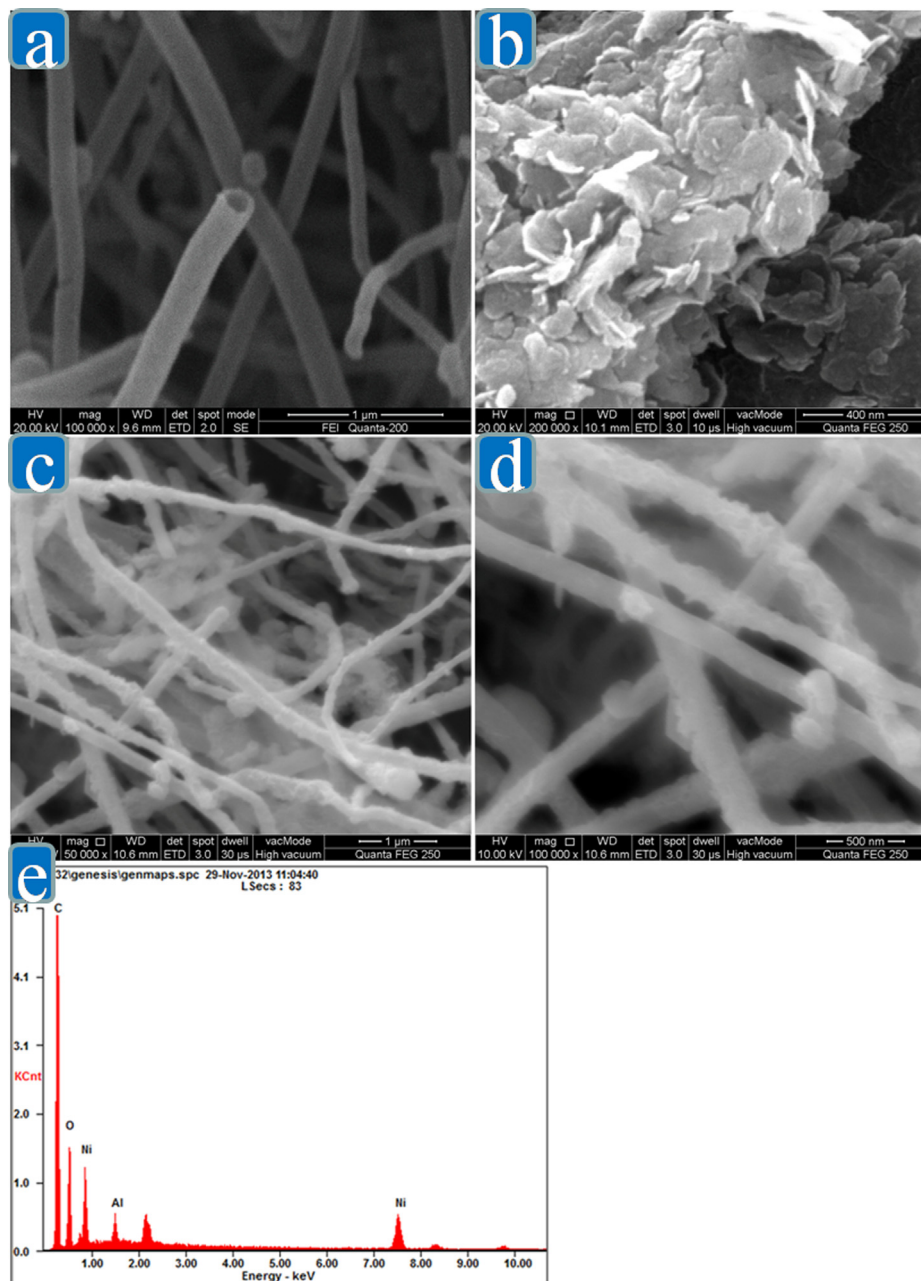


**Fig. 5.** SEM image of pristine CNFs (a), SEM image pure NiAl-LDH (b), SEM images of NiAl-LDH/CNFs composite (c, d), and EDS of the NiAl-LDH/CNFs composite (e).

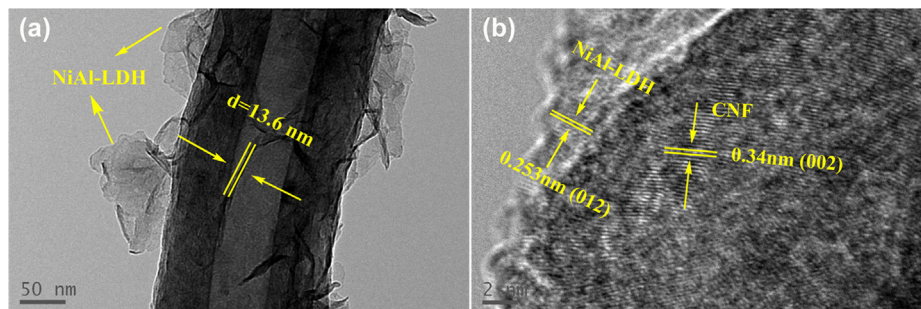


**Fig. 6.** TEM images of the NiAl-LDH/CNFs composite (a), and high-resolution TEM images of the composite (b).

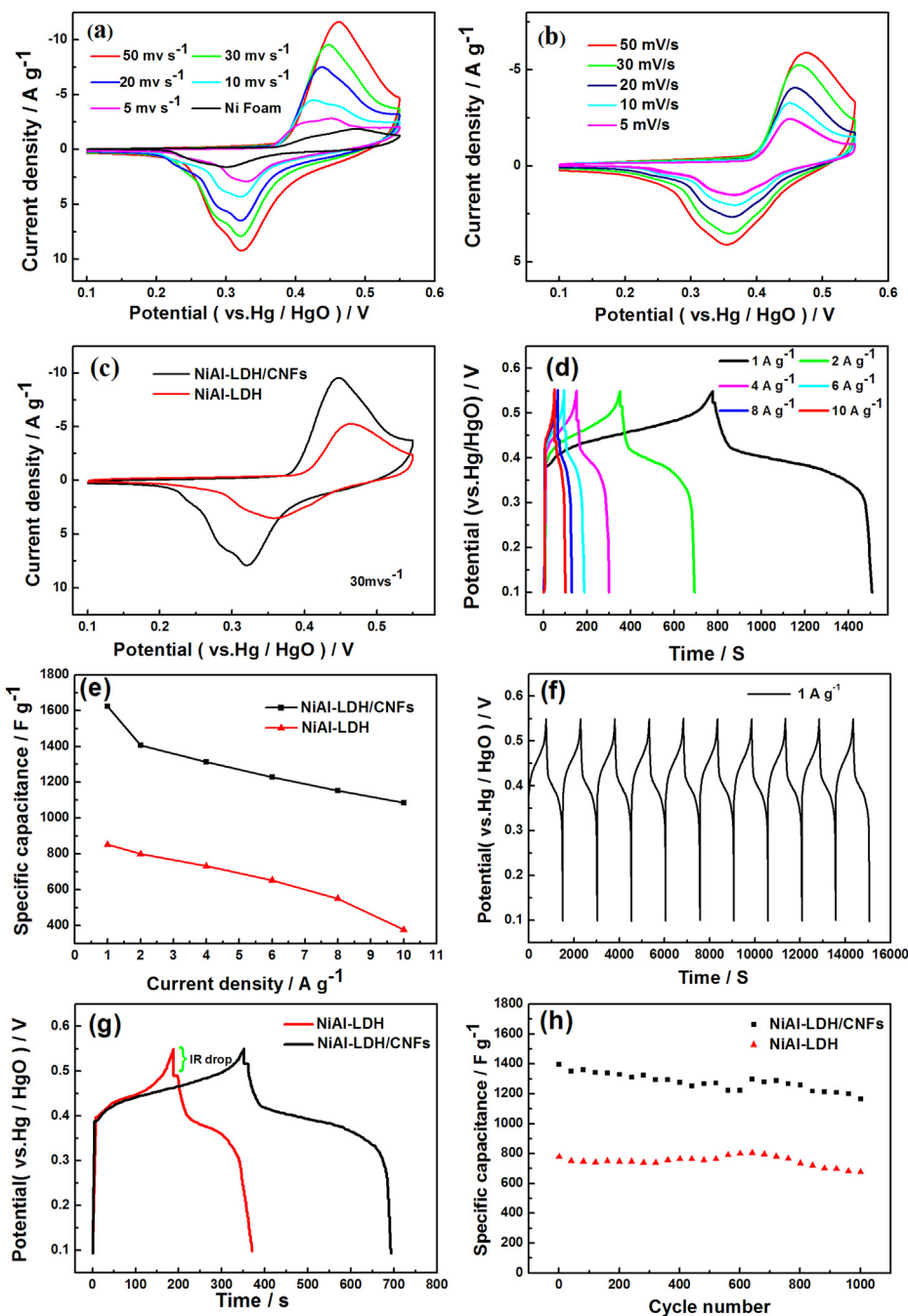


**Fig. 7.** (a) CV curves of the NiAl-LDH/CNFs composite at different scan rates, and the CV curve of the Ni foam (b) CV curves of the pure NiAl-LDH at different scan rates (c) CV curves of the NiAl-LDH and NiAl-LDH/CNFs composite at a scan rate of  $30 \text{ mV s}^{-1}$ , (d) charge–discharge curves of the composite at different current densities, (e) specific capacitance of the NiAl-LDH and NiAl-LDH/CNFs composite at different current densities, (f) charge–discharge curves of the composite electrode at a current density of  $1 \text{ A g}^{-1}$ , (g) charge–discharge curves for pure NiAl-LDH and NiAl-LDH/CNFs composite at  $2 \text{ A g}^{-1}$ , (h) cycling performances of the NiAl-LDH and NiAl-LDH/CNFs composite electrodes at a current density of  $2 \text{ A g}^{-1}$ .

where  $C_s$  is the specific capacitance ( $\text{F g}^{-1}$ ),  $I$  is the charge–discharge current (A),  $t$  is the discharge time (s),  $\Delta V$  is the potential window, and  $m$  is the mass of the active materials (g) [8]. The inset of Fig. 7d provide the specific capacitance of the NiAl-LDH/CNFs composite is calculated to be 1613, 1406, 1333, 1240, 1173, and  $1110 \text{ F g}^{-1}$  at different discharge current densities of 1, 2, 4, 6, 8, and  $10 \text{ A g}^{-1}$ , respectively. These values are much higher than those of pristine NiAl-LDH (853, 780, 732, 653, 551, and  $377 \text{ F g}^{-1}$  at the corresponding current densities) according to Fig. 7e. Moreover, our tests suggest that the composite electrode can still maintain

68.8% of the capacitance when the discharge current density is increased from 1 to  $10 \text{ A g}^{-1}$ . In comparison, the pure NiAl-LDH only maintains 44.2% of the capacitance, showing that the NiAl-LDH/CNFs composite has a better rate capability. This result further confirms that the contribution of CNFs in enhancing the specific capacitance, which can be attributed to good electrical conductivity and stable structure of CNFs.

To investigate the cycle performance of NiAl-LDH/CNFs composite, the galvanostatic charge–discharge curves of the NiAl-LDH/CNFs composite electrodes at a current density of  $1 \text{ A g}^{-1}$  were

obtained. Fig. 7f shows that each charge–discharge cycle approximately has a potential time response behavior, demonstrating that the composite has a good reversible stability. In Fig. 7g, the charge/discharge curves of the two samples were obtained at  $2 \text{ A g}^{-1}$ , the IR drop value of NiAl-LDH/CNFs composite is much smaller than that of NiAl-LDH, indicating the larger inner resistance of pure NiAl-LDH. Without doubt, this obvious IR drop difference was the evidence that the CNFs could improve the electronic conductivity of the NiAl-LDH.

The cycle performance of NiAl-LDH/CNFs composite and pure NiAl-LDH was also detected at the current of  $2 \text{ A g}^{-1}$  and the results are shown in Fig. 7h. The NiAl-LDH/CNFs composite has a higher specific capacitance of  $1164 \text{ F g}^{-1}$  over NiAl-LDH ( $677 \text{ F g}^{-1}$ ) after 1000 cycles. Meanwhile, the specific capacitance of the composite can still with the good retention of 83.4% after 1000 cycles, demonstrating the excellent long-term electrochemical stability of the composite.

To further understand the electrochemical behaviors of the as-prepared electrode materials, electrochemical impedance spectroscopy (EIS) measurements were used to investigate the electrode reaction kinetics of different samples. Fig. 8 shows that the Nyquist plots of both two samples contain a semicircle in high frequency region and a nearly straight line in the low frequency region. The high-frequency semicircle loop corresponds to the charge transfer resistance ( $R_{ct}$ ) of the electrode, and the slope in the low frequency region is may be caused by the diffusion of  $\text{OH}^-$  ions on the electrode material [20,44]. Typically, the semicircles can be attributed to charge transfer processes. Calculating the diameter of NiAl-LDH/CNFs composite and NiAl-LDH, it can be found that the NiAl-LDH/CNFs composite exhibit a much smaller charge transfer resistance ( $R_{ct} \approx 0.54 \Omega$ ) than the NiAl-LDH ( $R_{ct} \approx 6.75 \Omega$ ). At the same time, the slope of the line for NiAl-LDH/CNFs composite is larger than that of pure NiAl-LDH, indicating a lower ion diffusion resistance in the composite. This difference indicates that the CNFs play a significant role in the kinetics of the electrodes reactions, the linear carbon material can provide an effective conduction path of  $\text{Ni}^{2+}$  ions and an ideal network-like structure that forms a stable structure during the charge–discharge process. And the hollow structure might have sufficient space to prevent the agglomeration of active material and short transport length for ions diffusion. Therefore, the electrochemical performance of the composite electrode is apparently enhanced due to the synergistic effect of NiAl-LDH and the CNFs.

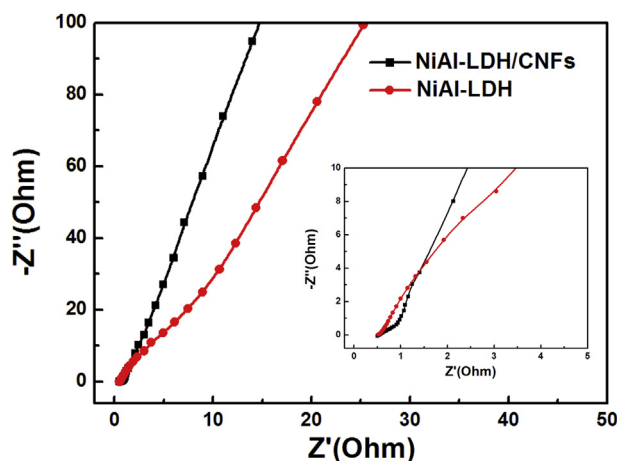


Fig. 8. Nyquist plots of the EIS for NiAl-LDH and NiAl-LDH/CNFs composite. Inset shows the impedance at high frequency region of the two samples.

#### 4. Conclusions

We have demonstrated that NiAl-LDH/CNFs composite was firstly successfully synthesized in our design. The NiAl-LDH nanosheets were grown vertically on CNFs to form three-dimensional porous structure includes ordered NiAl-LDH nanosheet arrays, high electroconductivity substrates. The large specific surface areas of the NiAl-LDH/CNFs composite, which can promote the interaction between electrolyte and active materials. The as-prepared composite demonstrates high specific capacitance, small charge transfer resistance and excellent cycle stability. These superior electrochemical performances is attributed to the CNFs addition that increases the electronic conductivity and specific surface area. Further optimization and control of the structures to exploit better electrochemical properties of CNFs based composites are under investigation. We hope that our attempt on NiAl-LDH/CNFs composite can bring a new idea for other people to explore new active electrode materials with good electrochemical performance as electrode material for supercapacitors.

#### Acknowledgments

This work was financially supported by the National Natural Science Foundation of China (21071153), Key Project of Hunan Provincial Science and Technology Plan of China (2014FJ2007).

#### References

- [1] J.R. Miller, P. Simon, *Science* 321 (2008) 651–652.
- [2] Z. Gao, J. Wang, Z. Li, W. Yang, B. Wang, M. Hou, Y. He, Q. Liu, T. Mann, P. Yang, M. Zhang, L. Liu, *Chem. Mater.* 23 (2011) 3509–3516.
- [3] P. Simon, Y. Gogotsi, *Nat. Mater.* 7 (2008) 845–854.
- [4] M.Q. Zhao, Q. Zhang, J.Q. Huang, F. Wei, *Adv. Funct. Mater.* 22 (2012) 675–694.
- [5] H. Jiang, P.S. Lee, C. Li, *Energy Environ. Sci.* 6 (2013) 41–53.
- [6] L. Zhang, J. Wang, J. Zhu, X. Zhang, K.S. Hui, K.N. Hui, *J. Mater. Chem. A* 1 (2013) 9046–9053.
- [7] J. Yang, C. Yu, X. Fan, Z. Ling, J. Qiu, Y. Gogotsi, *J. Mater. Chem. A* 1 (2013) 1963–1968.
- [8] L. Wang, D. Wang, X.Y. Dong, Z.J. Zhang, X.F. Pei, X.J. Chen, B. Chen, J. Jin, *Chem. Commun.* 47 (2011) 3556–3558.
- [9] J. Gamby, P.L. Taberna, P. Simon, J.F. Fauvarque, M. Chesneau, *J. Power Sources* 101 (2001) 109–116.
- [10] A. Malak-Polaczyk, C. Vix-Guterl, E. Frackowiak, *Energy Fuels* 24 (2010) 3346–3351.
- [11] T. Liu, W.G. Pell, B.E. Conway, *Electrochim. Acta* 42 (1997) 3541–3552.
- [12] J.W. Lang, L.B. Kong, W.J. Wu, Y.C. Luo, L. Kang, *Chem. Commun.* 35 (2008) 4213–4215.
- [13] J.G. Wang, Y. Yang, Z.H. Huang, F. Kang, *J. Power Sources* 224 (2013) 86–92.
- [14] X.H. Xia, J.P. Tu, Y.Q. Zhang, Y.Q. Mai, X.L. Wang, C.D. Gu, X.B. Zhao, *RSC Adv.* 2 (2012) 1835–1841.
- [15] X. Yan, Z. Tai, J. Chen, Q. Xue, *Nanoscale* 3 (2011) 212–216.
- [16] G.A. Snook, P. Kao, A.S. Best, *J. Power Sources* 196 (2011) 1–12.
- [17] Q. Xiao, X. Zhou, *Electrochim. Acta* 48 (2003) 575–580.
- [18] J. Pu, Y. Tong, S. Wang, E. Sheng, Z. Wang, *J. Power Sources* 250 (2014) 250–256.
- [19] K.M. Hercule, Q. Wei, A.M. Khan, Y. Zhao, X. Tian, L. Mai, *Nano Lett.* 13 (2013) 5685–5691.
- [20] C. Yu, J. Yang, C. Zhao, X. Fan, G. Wang, J. Qiu, *Nanoscale* 6 (2013) 3097–3104.
- [21] Z. Lu, W. Zhu, X. Lei, G.R. Williams, D. O'Hare, Z. Chang, X. Sun, X. Duan, *Nanoscale* 4 (2012) 3640–3643.
- [22] M. Li, J.E. Zhu, L. Zhang, X. Chen, H. Zhang, F. Zhang, S. Xu, D.G. Evans, *Nanoscale* 3 (2011) 4240–4246.
- [23] W. Chen, Z. Fan, L. Gu, X. Bao, C. Wang, *Chem. Commun.* 46 (2010) 3905–3907.
- [24] M. Liu, L. Gan, W. Xiong, Z. Xu, D. Zhu, L. Chen, *J. Mater. Chem. A* 2 (2014) 2555–2562.
- [25] M. Li, W. Xu, W. Wang, Y. Liu, B. Cui, X. Guo, *J. Power Sources* 248 (2014) 465–473.
- [26] J. Zhang, Y.S. Hu, J.P. Tessonier, G. Weinberg, J. Maier, R. Schlögl, D.S. Su, *Adv. Mater.* 20 (2008) 1450–1455.
- [27] S. Werner, V.W. Lau, S. Hug, V. Duppel, H. Clausen-Schaumann, B.V. Lotsch, *Langmuir* 29 (2013) 9199–9207.
- [28] G. Zou, D. Zhang, C. Dong, H. Li, K. Xiong, L. Fei, Y. Qian, *Carbon* 44 (2006) 828–832.
- [29] E. Hammel, X. Tang, M. Trampert, T. Schmitt, K. Mauthner, A. Eder, P. Pötschke, *Carbon* 42 (2004) 1153–1158.

- [30] A. Das, T.M. Schutzius, I.S. Bayer, C.M. Megaridis, *Carbon* 50 (2012) 1346–1354.
- [31] X.B. Cheng, G.L. Tian, X.F. Liu, J.Q. Nie, M.Q. Zhao, J.Q. Huang, W. Zhu, L. Hu, Q. Zhang, F. Wei, *Carbon* 62 (2013) 393–404.
- [32] L. Su, C. Ma, T. Hou, W. Han, *RSC Adv.* 3 (2013) 19807–19811.
- [33] M. Shao, F. Ning, J. Zhao, M. Wei, D.G. Evans, X. Duan, *J. Am. Chem. Soc.* 134 (2012) 1071–1077.
- [34] H. Chen, F. Zhang, S. Fu, X. Duan, *Adv. Mater.* 18 (2006) 3089–3093.
- [35] J.V. Walker, *J. Am. Chem. Soc.* 119 (1997) 6921–6922.
- [36] J. Wang, G. Fan, H. Wang, F. Li, *Ind. Eng. Chem. Res.* 50 (2011) 13717–13726.
- [37] M. Shao, F. Ning, Y. Zhao, J. Zhao, M. Wei, D.G. Evans, X. Duan, *Chem. Mater.* 24 (2012) 1192–1197.
- [38] Y. Zhao, S. He, M. Wei, D.G. Evans, X. Duan, *Chem. Commun.* 46 (2010) 3031–3033.
- [39] B. Sels, D.D. Vos, M. Buntinx, F. Pierard, A. Kirsch-De Mesmaeker, P. Jacobs, *Nature* 400 (1999) 855–857.
- [40] L. Zhang, X. Zhang, L. Shen, B. Gao, L. Hao, X. Lu, F. Zhang, B. Ding, C. Yuan, *J. Power Sources* 199 (2012) 395–401.
- [41] N. Yulian, L. Ruiyi, L. Zaijun, F. Yinjun, L. Junkang, *Electrochim. Acta* 94 (2013) 360–366.
- [42] Z. Wang, X. Zhang, J. Wang, L. Zou, Z. Liu, Z. Hao, *J. Colloid Interface Sci.* 396 (2013) 251–257.
- [43] L.H. Su, X.G. Zhang, Y. Liu, *J. Solid State Electrochem.* 12 (2007) 1129–1134.
- [44] J. Xu, S. Gai, F. He, N. Niu, P. Gao, Y. Chen, P. Yang, *J. Mater. Chem. A* 2 (2014) 1022–1031.
- [45] Z. Liu, R. Ma, M. Osada, N. Iyi, Y. Ebina, K. Takada, T. Sasaki, *J. Am. Chem. Soc.* 128 (2006) 4872–4880.
- [46] J. Fang, M. Li, Q. Li, W. Zhang, Q. Shou, F. Liu, X. Zhang, J. Cheng, *Electrochim. Acta* 85 (2012) 248–255.
- [47] H. Wang, X. Xiang, F. Li, *J. Mater. Chem.* 20 (2010) 3944–3952.
- [48] J. Wang, Y. Song, Z. Li, Q. Liu, J. Zhou, X. Jing, M. Zhang, Z. Jiang, *Energy Fuels* 24 (2010) 6463–6467.
- [49] F. Cheng, J. Liang, Z. Tao, J. Chen, *Adv. Mater.* 23 (2011) 1695–1715.